



Hydrodeoxygenation of guaiacol over halloysite nanotubes decorated with Ru nanoparticles: Effect of alumina acid etching on catalytic behavior and reaction pathways

Gleb Zasypalov ^a, Anna Vutolkina ^{a,b}, Vladimir Klimovsky ^a, Egor Abramov ^a,
Vladimir Vinokurov ^a, Aleksandr Glotov ^{a,*}

^a Gubkin Russian State University of Oil and Gas, 65 Leninsky Prospekt, 119991 Moscow, Russia

^b Lomonosov Moscow State University, 1-3 Leninskiye Gory, GSP-1, 119991 Moscow, Russia

ARTICLE INFO

Keywords:
Halloysite
Guaiacol
Dealumination
Hydrodeoxygenation
Bio-oil upgrading

ABSTRACT

Halloysite nanotubes (HNTs) is a promising support for liquid-phase hydrodeoxygenation (HDO) catalysts due to a wide abundance, low cost and tunable properties. Acid etching of halloysite by sulfuric acid was found to enlarge lumen diameter (24.3 nm), enhance specific surface area (154 m²/g) and acidity (0.343 mmol/g). Based on pristine and dealuminated HNTs, Ru-containing catalysts were synthesized via impregnation under microwave irradiation. The catalytic properties of synthesized catalysts in HDO of guaiacol were studied in batch reactors at 120–180 °C, under hydrogen pressure of 3 MPa, with guaiacol/Ru molar ratio of 200 in water as a solvent. Comparing the results of catalytic tests, we have concluded that the catalysts based on etched halloysite enhanced greater activity (TOF – 211 h⁻¹) in the HDO of guaiacol compared their analogue supported on pristine HNTs. Moreover, the Ru-catalyst based on etched HNTs contributed to an increase selectivity to hydrogenolysis with effective oxygen removal.

1. Introduction

In the last decade, there has been a growing interest in liquid fuels production and petrochemicals from bio-oils produced by pyrolysis of lignocellulosic biomass. Wood wastes are promising biological raw materials because their processing involves CO₂ capture from the atmosphere and allows production of biofuel with characteristics similar to those for motor fuels. However, lignocellulosic biomass-derived bio-oil is characterized by a high concentration of wide-variety oxygen-containing compounds, which limits its application as a fuel due to high corrosiveness (TAN - 100 mg KOH kg⁻¹), a low mass calorific value (16–19 MJ/kg), a high viscosity and a tendency to polymerization-condensation [1]. Typically, bio-oils contain up to 40–50 wt% of oxygen [2]. Oxygen removal and water separation for improving the quality of bio-oil is required before its involvement into refinery with hydrocarbon feed using standard equipment and traditional catalysts. A promising technology for processing of bio-oil is catalytic hydrotreatment, i.e. hydrodeoxygenation (HDO), where bio-oil components undergo decarboxylation, decarbonylation, cracking and hydrogenation

thereby increasing hydrocarbon content.

For bio-oil produced by fast pyrolysis of plant biomass, the content of phenolic compounds and its derivatives as lignin-derived building blocks reaches ca. 40%. Among them, guaiacol is considered a typical model compound for testing catalysts in HDO due to the presence of two types of C-O bonds (Csp₂OCH₃ and Csp₂OH) in its structure [3,4]. The HDO reaction mechanism is very complex, but generally two pathways are suggested. The first one is HDO, which includes hydrogenation followed by C-O bond scission [5], whereas the second one is C-O bond cleavage called direct deoxygenation (DDO) or hydrogenolysis [6]. The HDO pathway requires a bifunctional catalyst with active metal sites for hydrogenation and acidic function for deoxygenation via dehydration. Some researchers reported that synergism between Lewis acid sites and metallic nanoparticles is the main factor for increasing catalyst' activity in the two-step hydrogenolysis of phenolic compounds due to better adsorption on aluminium species [7,8].

Up to now three types of catalysts for bio-oil upgrading have been developed: traditional NiMo/Al₂O₃ and CoMo/Al₂O₃ sulfide hydro-treating catalysts; heterogeneous catalysts based on transition metals

* Corresponding author.

E-mail address: glotov.a@gubkin.ru (A. Glotov).



(Ni, Co, Fe) oxides and noble metal (Rh, Ru, Pt and Pd) catalysts [9–12]. Catalysts comprising transition metal oxides and sulfides demonstrate some disadvantages, such as sulfur loss from metal sulfides and phase changes of metal oxides resulting in low HDO activity [13]. Compared to transition metal-based catalysts, noble metal-containing counterparts show better hydrogenation of aromatic rings in the HDO process [14]. Catalysts based on noble metals, in particular those containing Ru, are almost devoid of disadvantages. These catalysts exhibit a high hydrogenation and hydrogenolysis activity even in the presence of water which is produced in large amounts during HDO of bio-oil [15,16]. The major benefits of noble metal catalysts are high stability to coke deposition and regenerability under hydrogen pressure without any treatment unlike for transition metal sulfides. However, when zeolites as the most common supports are used, the coke formation occurs even for noble metal-based catalysts. Additionally, for microporous acidic zeolite-supported catalysts the diffusion limitations during the sorption of substrate molecules whose size exceeds the pore diameter of the supports is acknowledged as the main disadvantage [17,18]. This factor leads to a decrease in catalytic activity due to the limited access to the active sites for large substrate molecules. Moreover, the high acidity of microporous materials increases the yield of by-products formed by cracking and condensation [19].

As a support for hydrodeoxygenation catalysts, natural clay nanotubes such as halloysite are of a particular interest. Halloysite nanotubes (HNTs) are formed by rolling of kaolin sheets into the tubes with length of ca. 0.5–2 μm with negatively charged outer surface consisting of tetrahedral silanol groups and positive charged inner surface composed of octahedral alumina groups [20]. Halloysite has an appropriate specific surface area (60–100 m^2/g), high ion-exchange capacity and mesoporous structure. The unique feature of halloysite nanotubes is a 12–20 nm diameter lumen formed by aluminosilicate sheets: this lumen can be loaded with metal nanoparticles providing formation of well dispersed active phase, which allows for highly active HDO catalysts [21].

However, to the best of our knowledge regarding application of HNTs in catalysis [22–25], we have high confidence that the low concentration of acid sites (0.1–0.2 mmol/g) of halloysite more likely would favor HDO via hydrogenation of oxygen-containing compounds without hydrogenolysis and isomerization reaction pathways. It is a significant drawback in terms of oxygen removal, and there are many ways for HNTs modification to enhance their textural and acidic properties for increasing HDO activity. It was thoroughly investigated for aluminosilicates, that structural defects, which are created by dealumination with acid treatment, leads to an increase the concentration and strength of acid sites. For HNTs, selective acid etching appears to be a promising method to increase the strength of acid sites by breaking covalent bonds and releasing isolated aluminum atoms with the formation of new Si-O-Al-OH sites [21]. Moreover, due to the alumina is a component of inner cavity, acid etching would increase the lumen diameter, which improves mass transfer and enhance capacity of internal surface for loading of metal nanoparticles. Defects in the halloysite nanotubes' layers, when ordered tubular structure retaining, allows for improving textural characteristics such as specific surface area (up to 200 m^2/g) and average pore diameter (due to the formation of new through pores) [26–28]. In view of layered tubular structure of HNTs, the structural, acidic and physico-chemical properties of HNTs vs. acid treatment conditions is of particular interest.

Herein, we have studied the effect of acid dealumination kinetic process for natural aluminosilicate HNTs on their structural, acidic and textural properties to select the more appropriate candidate as the support for Ru-containing HDO catalysts. We have also evaluated the effect of HNTs support on reaction pathway for liquid-phase HDO of guaiacol as a model component of lignin-derived bio-oil over Ru-catalysts in aqueous media. This work can provide the theoretical references for the upgrading of lignin-derived bio-oil over acid-etched halloysite nanotubes decorated with noble metals.

2. Material synthesis and method

Ruthenium chloride (III) (45–55% Ru), guaiacol ($\geq 99\%$), sodium borohydride (85%) and halloysite nanotubes (HNTs) were purchased from Sigma-Aldrich, sulfuric acid (98% H_2SO_4) and ethanol were purchased from Ekos-1, (Russia). Pure gases (Ar, H_2 , He, N_2) were supplied by NIIKM (Russia). All the chemicals were used as received without further purification.

2.1. Acid etching of HNTs

Acid etching was carried out in order to selective removal of alumina from that composed the interior space of HNTs. 20 g of HNTs were treated with 230 mL of 2 M H_2SO_4 solution and temperature of 65 °C under intensive stirring for 6–24 h. After the treatment was terminated, the suspension was filtered, washed with distilled water until the pH 6–7 and then dried at 110 °C overnight. Finally, the HNTs were calcined at 600 °C in air prior to further characterization. The as-prepared supports were named as HNT-t (n), where n depends on time of acid treatment: n = 1; 2; 3; 4; 5 for 6 h; 12 h; 16 h; 18 h; 24 h, respectively.

2.2. Catalysts preparation

Ruthenium catalysts with 2 wt% metal loading were synthesized by wetness impregnation under microwave irradiation. In account of the structural, textural properties and acidity, the HNT-t (3) support was selected as a promising candidate for Ru-supported catalysts of guaiacol HDO. According to the typical procedure, calculated amount of ruthenium chloride (III) was dissolved in 20 mL of distilled water. The solution was added to 1 g of the support (pristine HNTs or acid-etched HNTs), the obtained mixture was sonicated for 40 min and treated under microwave radiation at 800 W for 10 min. The resulted solid powder was centrifuged and the supported Ru^{3+} was reduced to Ru^0 using 0.5 M sodium borohydride solution (in excess amount). After reduction procedure, the nanoclay-supported Ru catalysts were centrifuged, washed with distilled water (3 times) and ethanol (2 times) to remove products of sodium borohydride decomposition. The resulting catalysts samples were dried for 24 h at room temperature and stepwise at 80, 90, 110 and 140 °C for 2 h at each temperature. The as-prepared catalysts were denoted as Ru/HNT and Ru/HNT-t (3), respectively.

2.3. Characterization of supports and catalysts

Transmission electron microscopy (TEM, JEOL, JEM-2100) was applied to investigate structure and morphology of supports and catalysts. The samples were dispersed in ethanol, afterwards placed on the copper grid and analyzed under an accelerating voltage of 200 kV. Also, this method was used to estimate size and distribution of Ru particles in the reduced catalysts. The particles size was calculated using ImageJ software.

Textural characteristics (specific surface area (S_{BET}), volume and diameter of pores) were determined by low-temperature nitrogen adsorption/desorption using a Gemini VII 2390 t instrument (Micromeritics, USA) at $-196\text{ }^\circ\text{C}$. Prior to the analysis, the samples were outgassed at 300 °C for 4 h. The S_{BET} values were calculated by application of the Brunauer-Emmett-Teller theory equation to the nitrogen adsorption data. The volume of pores and their diameter were estimated in terms of the Barret-Joyner-Halenda model.

Hydrogen temperature-programmed reduction (H_2 -TPR) was carried out on an AutoChem HP2950 (Micromeritics, USA) instrument equipped with a thermal conductivity detector (TCD). Before experiments, the catalysts were calcined in the air flow at 400 °C for 4 h to convert ruthenium into an oxide form. $\sim 0.1\text{ g}$ of the catalyst powder was placed in a quartz reactor and kept in the argon flow at 400 °C for 1 h. Then the reactor was cooled down to 60 °C, and the sample was heated in the 8% $\text{H}_2 + \text{Ar}$ gas mixture (30 mL/min) at 10 °C/min up to 400 °C.

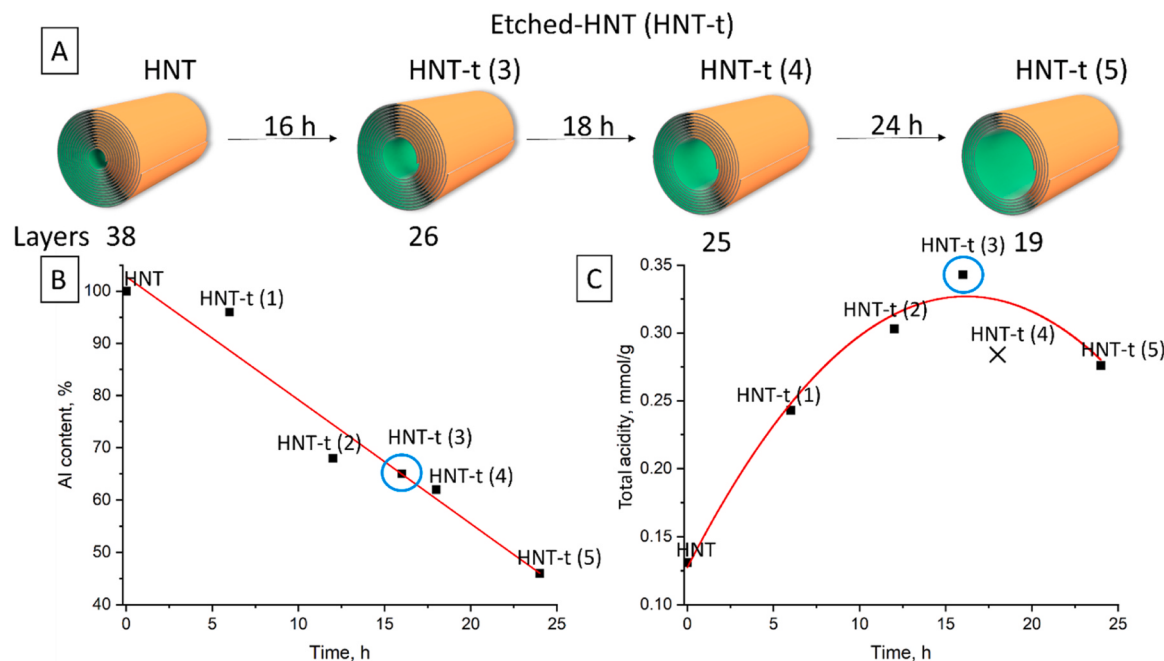


Fig. 1. Illustration of the dealumination process with a decrease in the number of aluminosilicate layers (A), Normalized Al content in halloysite depending on time of acid etching (B), Total acidity of the etched HNTs as a function of time of acid treatment (C).

The elemental compositions of the supports and catalysts were determined by energy-dispersive X-ray fluorescence (XRF) spectroscopy on an ARL Perform'X instrument (Thermo Fisher Scientific). The results were processed using the UniQuant standardless method.

The catalysts and the supports were characterized by ammonia temperature-programmed desorption ($\text{NH}_3\text{-TPD}$) procedure on AutoChem HP2950 instrument. Ammonia adsorption was carried out in a quartz reactor at 60°C for 30 min. Physically adsorbed NH_3 was removed in a nitrogen flow at 100°C for 30 min. The change of ammonia concentration in the effluent gas, upon heating samples from 100° to 700°C with a ramp of $10^\circ\text{C}\cdot\text{min}^{-1}$ was analyzed with a TCD as a function of temperature.

Fourier transform infrared (FTIR) spectra of adsorbed pyridine were recorded on a Shimadzu IRTtracer-100 FTIR spectrometer at 4 cm^{-1} resolution. Prior to the measurements, the sample was pressed into self-supporting discs and activated in the cell attached to a vacuum line at 400°C for 2 h. Adsorption of pyridine was performed at 150°C for 30 min at 2 torr. Following this, pyridine was evacuated at 150°C . After that, the temperature was raised by 50°C every 15 min and the amount of desorbed pyridine was determined. A number of Brønsted and Lewis acid sites was determined by the absorption bands at 1545 and 1450 cm^{-1} respectively.

2.4. Catalytic activity tests

Evaluation of the catalytic activity in HDO of guaiacol was performed in a 5000 Multiple Reactor System (Parr Instruments, USA) with stainless steel batch reactors, teflon insets, equipped with magnet bars. A reactor was loaded with 61 mg of a catalyst and 3 g of model feed (10 wt % of guaiacol in distilled water). The substrate/Ru molar ratio was kept constant at the value of 200. The reactors were sealed and filled with hydrogen to the pressure of 3 MPa. Catalytic tests were performed in a temperature range of $120\text{--}180^\circ\text{C}$ for 3 h. The reaction time was kept, when the designated temperature was set. Once a catalytic test was finished, a reactor was cooled down to room temperature and depressurized, then solid powder was separated from liquid products by centrifugation. HDO liquid products were analyzed in isotherm (200°C) using a Chromos GC-1000 gas chromatograph (Chromos Engineering,

Russia) equipped with a flame-ionization detector and a capillary column MEGA-WAX Spirit (MEGA, Italy). The individual components were identified by GC-MS analysis (Thermo Scientific Trace GC Ultra). The chromatograph was equipped with a HP-5MS capillary column ($30\text{ m} \times 0.25\text{ mm} \times 0.25\text{ }\mu\text{m}$). Blank experiments using only halloysite supports were also carried out under the same conditions. Mass-balance was closed in 98–99%, gaseous products were detected in trace amount.

2.5. Product analysis

Guaiacol conversion, selectivity to reaction products and turnover frequency were calculated as follows:

$$\text{Conversion } (\%) = 100\% - N_{\text{Gua}} \quad (1)$$

$$\text{Selectivity } (\%) = \frac{N_i}{\sum N_i - N_{\text{Gua}}} \cdot 100\% \quad (2)$$

where N_{Gua} and N_i denote as molar concentrations of guaiacol and other components in reaction products, which were calculated using an absolute normalization method taking into account the relative response factor f calculated as follows:

$$N_i \quad (\%) = \frac{S_i \cdot f_i^{-1}}{\sum S_i \cdot f_i^{-1}} \cdot 100\% \quad (3)$$

where S_i is a peak area of each product determined by GC coupled with a FID detector. The FID calibration response factors f_i were calculated by analyzing the gas chromatograms of standards. Cyclohexanol was used as an etalon component ($f=1$). The other factors were found as the ratio of peak areas of the reaction product to the peak area of cyclohexanol. For this, 3 solutions were prepared with a give molar ratio. Each solution was analyzed by GC at least 3 times, and the factor values were found as the arithmetic average [29]. The results obtained are presented in Table S1.

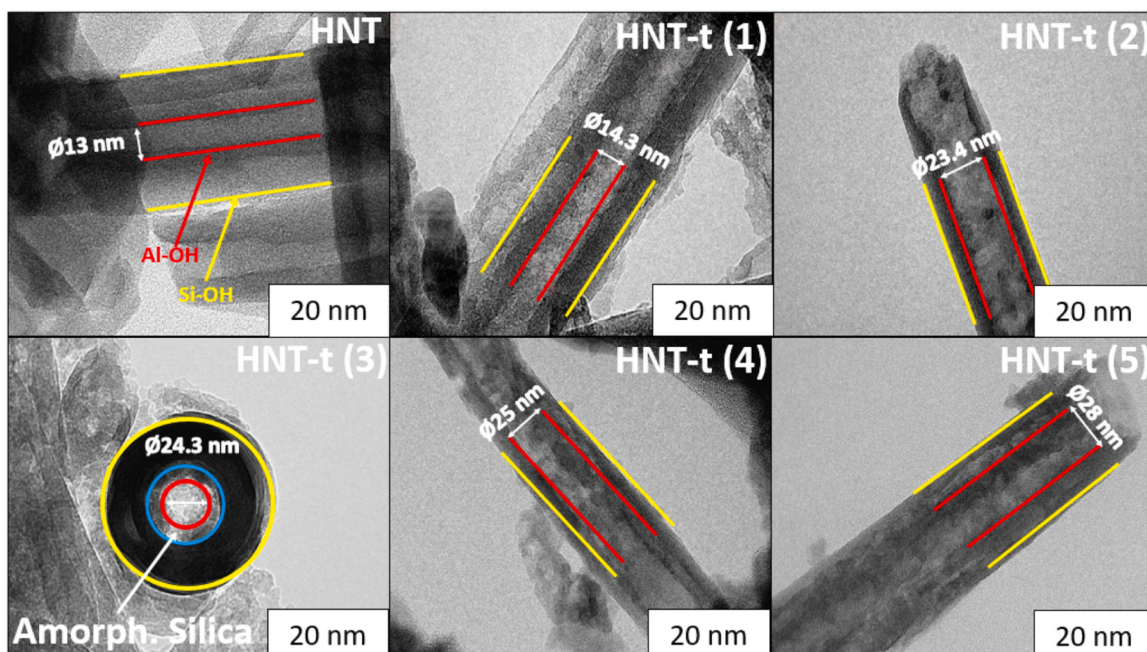
Turnover frequency (TOF) was calculated as follows:

$$\text{TOF } (h^{-1}) = \frac{\text{Conversion}_{\text{Gua}} \cdot v_{\text{Gua}}}{v_{\text{Ru}} \cdot t} \quad (4)$$

Table 1

Physicochemical properties and parameters of halloysite dealumination.

Sample	Time, h	Al, % ^a	Si/Al	Lumen diameter, nm	Average layers	Weak acid sites, mmol/g	Medium and strong acid sites, mmol/g	Total acidity, mmol/g
HNT	0	100	0.91	13.00	38	0.131	-	0.131
HNT-t (1)	6	96	1.01	14.35	37	0.083	0.160	0.243
HNT-t (2)	12	68	1.72	23.42	27	0.092	0.211	0.303
HNT-t (3)	16	65	1.86	24.29	26	0.098	0.246	0.343
HNT-t (4)	18	62	2.03	25.00	25	0.086	0.198	0.284
HNT-t (5)	24	46	3.07	27.93	19	0.094	0.182	0.276

^a According the X-ray fluorescence analysis data relative to pristine HNT**Fig. 2.** TEM images of pristine and acid-etched HNTs. *Conditions of etching: 65°C, 6–24 h, 2 M sulfuric acid solution.*

where v_{Ru} is an amount of moles of active phase in a catalyst, v_{Gua} is an amount of guaiacol moles in the feedstock and t is a reaction time.

3. Results and Discussion

3.1. Acid etching process

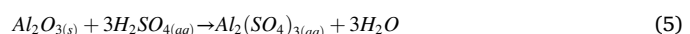
HDO is a complex process including two types of reactions: hydrogenation on metal sites and direct deoxygenation of functional groups on provided by acidity of a support. Pristine HNTs have got low concentration of acid sites (0.1–0.2 mmol/g). This fact imposes some restrictions for application of halloysite in HDO processes, in particular, due to ineffectiveness of C–O bond hydrogenolysis (deoxygenation). Acidity of HNTs can be selectively increased by acid etching, which also allows to enhance the inner diameter of the tubes by dealumination. The lumen diameter of HNTs can be regulated by changing time, temperature of treatment and acid concentration [26]. Moreover, acid etching of HNTs can improve the tube lumen capacity and favors loading of metal nanoparticles into the inner surface.

Fig. 1 A schematically represents the decrease in the number of aluminosilicate layer in HNTs with time on acid treatment. The kinetics of halloysite dealumination process using sulfuric acid solution (2 M) is depicted in Fig. 1B. A typical halloysite tube with an external diameter of 60–70 nm and a lumen diameter of 13 nm includes on average 35–40 aluminosilicate layers.

After acid etching, there are 26, 25 and 19 layers left (Fig. 1A). These

data correspond to the Al content in the samples obtained after dealumination (Fig. 1B, Table 1). The Al content in each aluminosilicate layer has been decreased from the inner shell layer-by-layer, followed by the enlargement of lumen diameter up to 28 nm (Fig. 2, Table 1). For all samples, acid etching led to an increase in the Si/Al molar ratio from 0.91 to 3.07, i.e., the Si content increases at the expense of Al (Table 1).

The decrease in alumina content for acid-treated samples could be explained by the release of Al species from the octahedral sheets according to the following reaction [30]:



The structures of the pristine and acid-etched halloysite were revealed by TEM analysis. A clear crystal morphology with a relatively small lumen diameter in the pristine halloysite was verified (Fig. 2).

For acid-etched halloysite the crystallinity decreases gradually with time of treatment, but was not completely lost after dealumination, and lumen diameter of nanotubes was expanded. However, the rod-like structure was preserved even after 54% removal of the alumina from halloysite (Fig. 2, Table 1). The external diameters of the tubes remained unchanged, indicating that etching affects the inner space solely.

NH₃-TPD profiles of the pristine and acid-etched HNT (HNT-t) are shown in Fig. S1. There are two major ammonia desorption peaks: first one is in the low temperature area (150–200 °C), which corresponds to weak acid sites, whereas the second one in the high temperature region (320–400 °C) is assigned to medium and strong acid sites. The total acidity reaches maximum value (0.343 mmol/g) after 16 h of acid

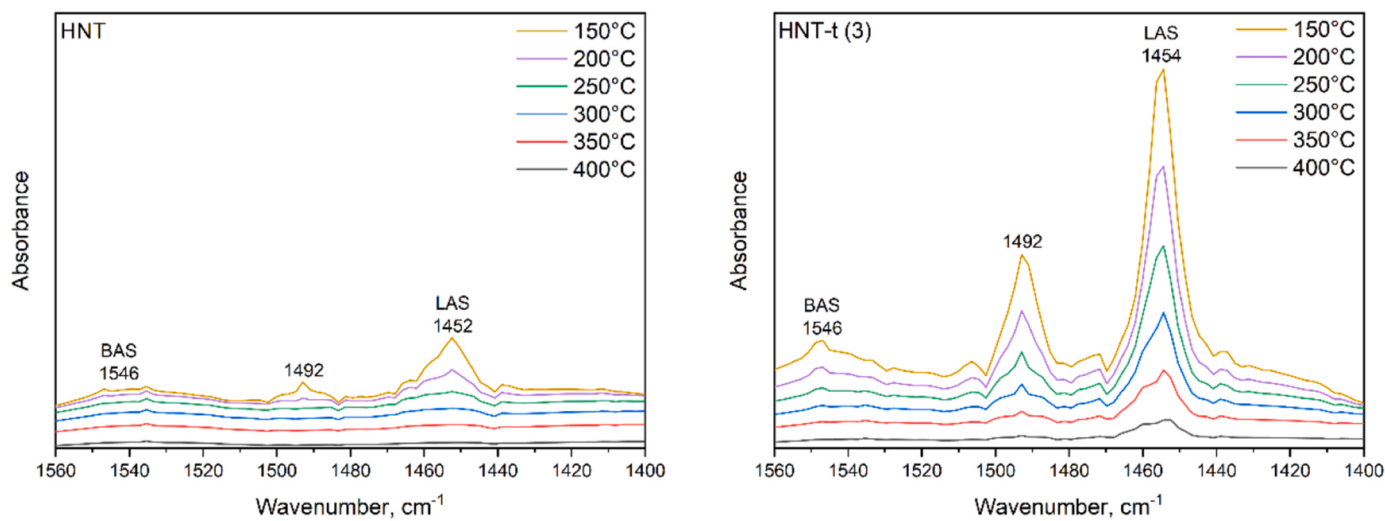


Fig. 3. Pyridine adsorption FTIR spectra of pristine HNT and acid-etched HNT-t (3) sample.

Table 2

Quantification of the Brønsted and Lewis acid sites ($\mu\text{mol/g}$) of pristine HNT and acid-etched HNT-t (3) sample by FTIR of pyridine adsorption.

Temperature	HNT				HNT-t (3)			
	Adsorption		Desorption		Adsorption		Desorption	
	BAS	LAS	BAS	LAS	BAS	LAS	BAS	LAS
150 °C	15	36	7	16	32	96	9	21
200 °C	8	20	8	8	23	75	7	12
250 °C	0	12	0	4	16	63	3	12
300 °C	0	8	0	3	13	51	0	15
350 °C	0	5	0	3	13	36	1	12
400 °C	0	2	0	2	12	24	11	23

treatment (Table 1). Apparently, this increase in acidity is caused by aluminol Al-OH species formed in the inner surface and when being protonated by H^+ ions form AlO^+H_2 species. As a result, the Al-O bonds in the aluminosilicate framework of halloysite become weaker with lability of oxygen atom increases at $\text{pH} = 1$ it favors rupture of Al-O bonds and escape of Al^{3+} ions from the framework. But before the

final structural collapse, the interatomic bonds are rearranged, the isolated aluminum atoms are released and Si-O-Al-OH_{1-2} type fragments with protons are formed [21,26,28]. As a result, peaks corresponding to strong acid sites appear on the NH_3 -TPD profile. Along with the acid etching process, the Al content decreases and Si-O-Al bonds breaks, which leads to decrease in acidity (Table 1).

This explanation corresponds with the results of pyridine adsorption FTIR spectroscopy (Fig. 3, Table 2). The signals at 1545 and 1450 cm^{-1} are attributed to BAS and LAS, respectively. Meanwhile, the adsorption band at 1492 cm^{-1} belongs to the combination of BAS and LAS and was not accounted for calculation [31,32].

Acid leaching of pristine HNTs leads to increase the number of Brønsted (BAS) and Lewis (LAS) acid sites by 2 and 3 times respectively (Table 2). Meanwhile, according to TPD- NH_3 data the total acidity also increased upon 3 times from 0.131 mmol/g to 0.343 mmol/g (Table 1, Fig. S1). Apparently, this difference in acidic properties of pristine HNT and acid-etched sample is caused by the release of isolated aluminum atoms from the halloysite framework, which leads to the formation of acid sites. Moreover, for the pristine HNT the pyridine desorption was completed at 350 °C, whereas for acid-etched HNT-t (3) counterpart a

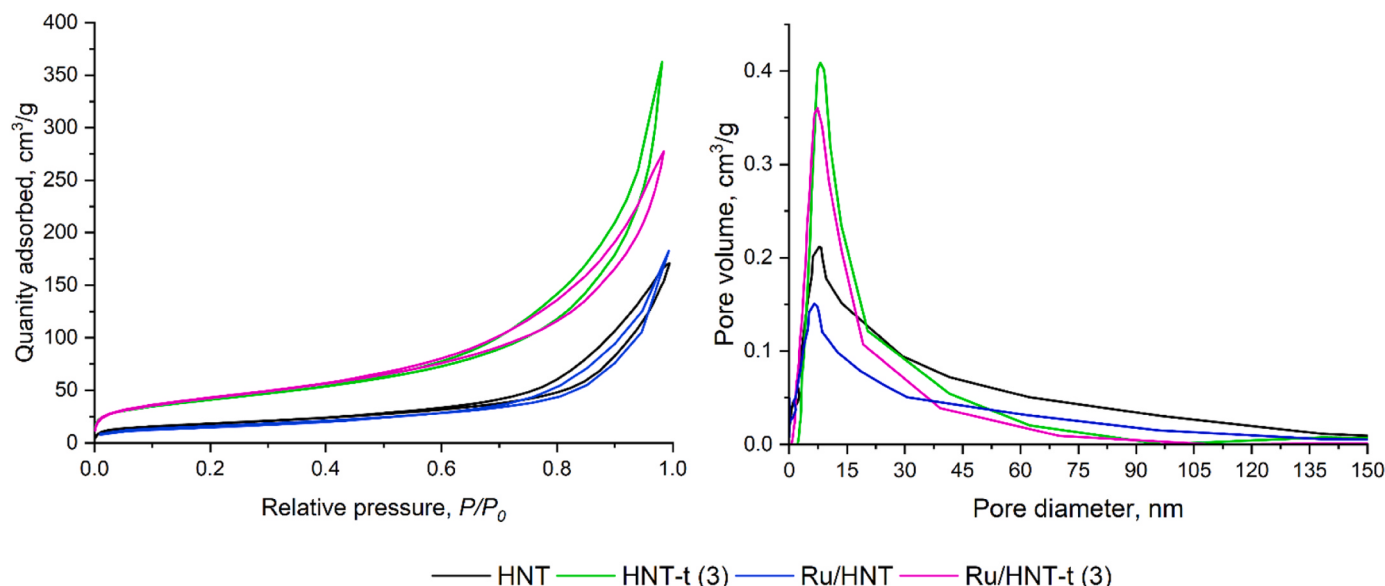


Fig. 4. N_2 adsorption-desorption isotherms for the halloysite supports and Ru-catalysts.

Table 3

Composition and textural characteristics of supports and catalysts based on pristine and acid-etched halloysite.

Sample	Chemical composition, wt%				Textural characteristics		
	Ru	Si	Al	Na	S_{BET} , m ² /g	Pore volume, cm ³ /g	Pore diameter, nm
HNT	-	23.6	26.1	0.06	67	0.21	8.2
HNT-t (3)	-	31.4	16.9	0.02	154	0.40	11
Ru/HNT	1.7	21.1	24.1	0.02	65	0.16	7.1
Ru/ HNT-t (3)	2.0	29.6	15.9	traces	137	0.35	9.3

*From the X-ray fluorescence analysis

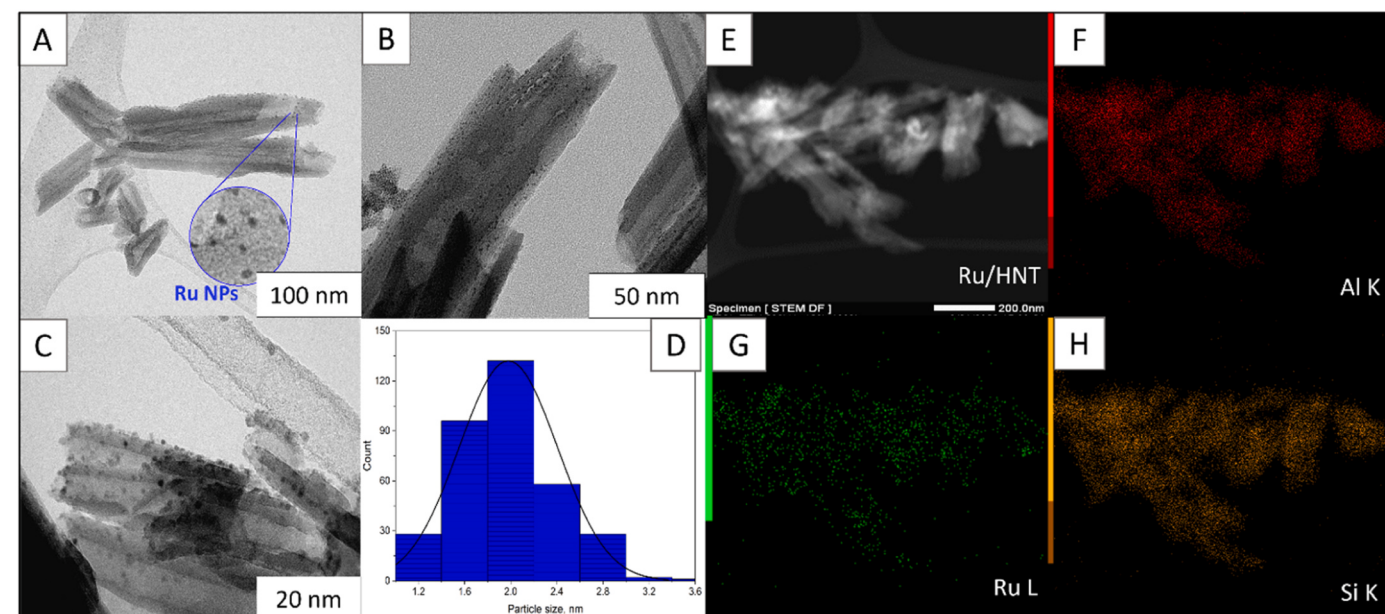


Fig. 5. TEM images (A-C), particle size distribution (D) and elemental mapping (F-H) for Ru/HNT catalyst.

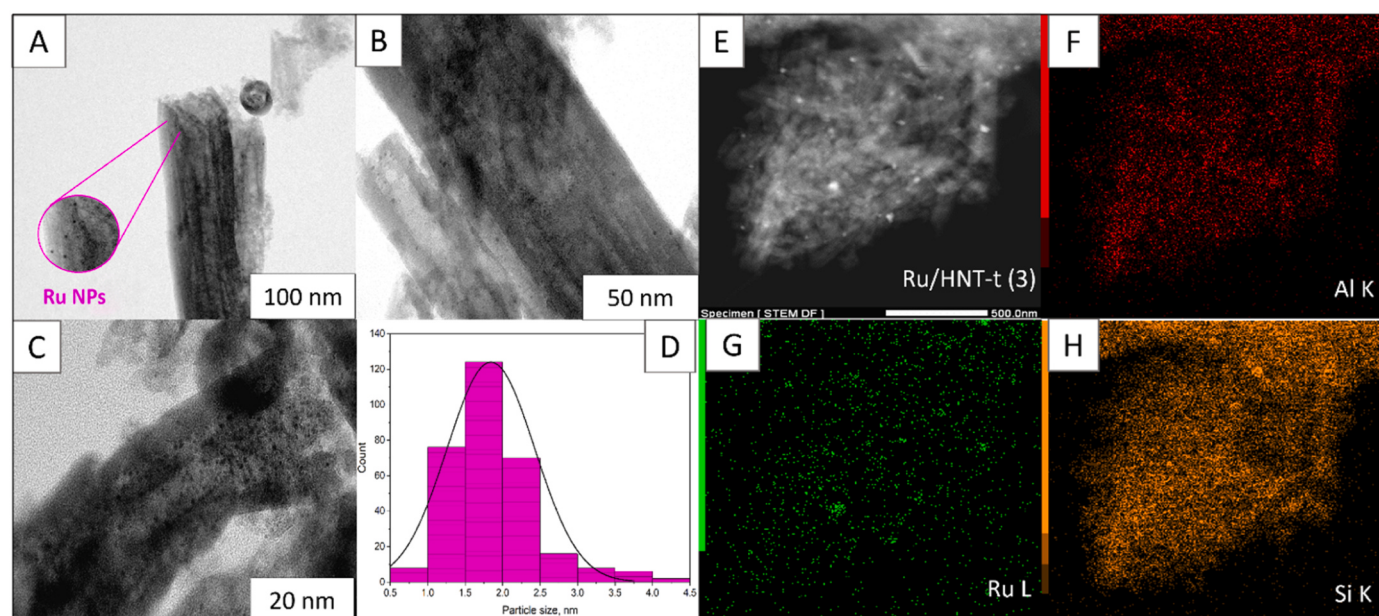


Fig. 6. TEM images (A-C), particle size distribution (D) and elemental mapping (F-H) for Ru/HNT-t (3) catalyst.

Table 4**H₂-TPR data of Ru-catalysts based on HNT and HNT-t (3).**

Sample	Temperature of reduction, °C	H ₂ consumption for RuO _x reduction, mmol/g	Ru content, wt%
Ru/HNT	132	0.364	1.82
Ru/HNT-t (3)	157	0.399	2.02

support and Ru-catalyst were in the range of 2–20 nm with an average value of 8.2 and 7.1 nm, for HNT and Ru/HNT, respectively. The acid etching increased these parameters up to 11 and 9.3 nm, respectively. The hysteresis loop indicates the presence of through cylindrical pores.

As seen from Table 3, HNT-t (3) sample significantly exceeds the pristine halloysite in its characteristics. The acid etching of HNTs leads to enlargement of pore volume and pore diameter up to 0.4 cm³/g and 11 nm, respectively. The acid treatment causes the removal of Al³⁺ from octahedral sheets thereby decreasing the number of aluminosilicate layers. It leads to formation of "holes" (through pores) in the halloysite framework, and ensures the accessibility of internal surface [34]. Specific surface area of the tubes increased more than two times (up to 154 m²/g) upon 35% of the dealumination, which is associated with the formation of defects in the structure of halloysite as a result of etching. After impregnation of Ru from RuCl₃ aqueous solution and drying, the samples generally demonstrated a small decrease of the adsorption capacity in respect to the corresponding supports (Table 3).

Metal impregnation from an aqueous solution of ruthenium salt under microwave irradiation provides highly dispersed catalysts with Ru nanoparticles of 1.5–2.7 nm, uniformly distributed over the outer

support surface and loaded into the lumen of HNTs (Figs. 5, 6). This Ru intercalation was not typical due to the positive charge of the lumen usually prevents ruthenium cations migration into the inner space of hollow tubes. The particle size distribution determined from the measurement of more than 300 particles reveals that the average particle size was about 2 nm for the both catalysts, whereas larger particles (up to 4 nm) are presented in a small amount. For Ru/HNT sample a maximum at 1.8–2.0 nm on distribution curve was observed (Fig. 5). In this case, the nanoparticles were mainly localized on the outer nanotube's surface. This was also confirmed by the low-temperature nitrogen adsorption-desorption: the specific surface area of the sample almost unchanged after metal deposition (Table 3). At the same time, the specific surface area of Ru/HNT-t (3) sample synthesized from dealuminated halloysite decreases from 154 m²/g to 137 m²/g, which is due to a higher metal content in this catalyst (Table 3). In this case, the active metal phase is localized evenly both on the outer and inner surfaces. Apparently, the acid etching provides an increase of the active phase loading to the inner cavity of HNTs, not only due to the enlarged lumen diameter, but also because of no difference in surface potential for the inner and outer halloysite surfaces [21,35,36]. In addition, the relatively high concentration of ruthenium nanoparticles in the inner cavity of the nanotubes can be associated with the formation of a large number of acid sites after alumina etching. Notably, that no effect of ruthenium reduction with NaBH₄ on sodium interaction with acid sites was observed. Moreover, the Na content in catalyst sample decreases after reduction procedure (Table 3). For Ru/HNT-t (3) catalyst, the average nanoparticle size was 1.5–2.0 nm, which is comparable to that for the sample based on pristine halloysite.

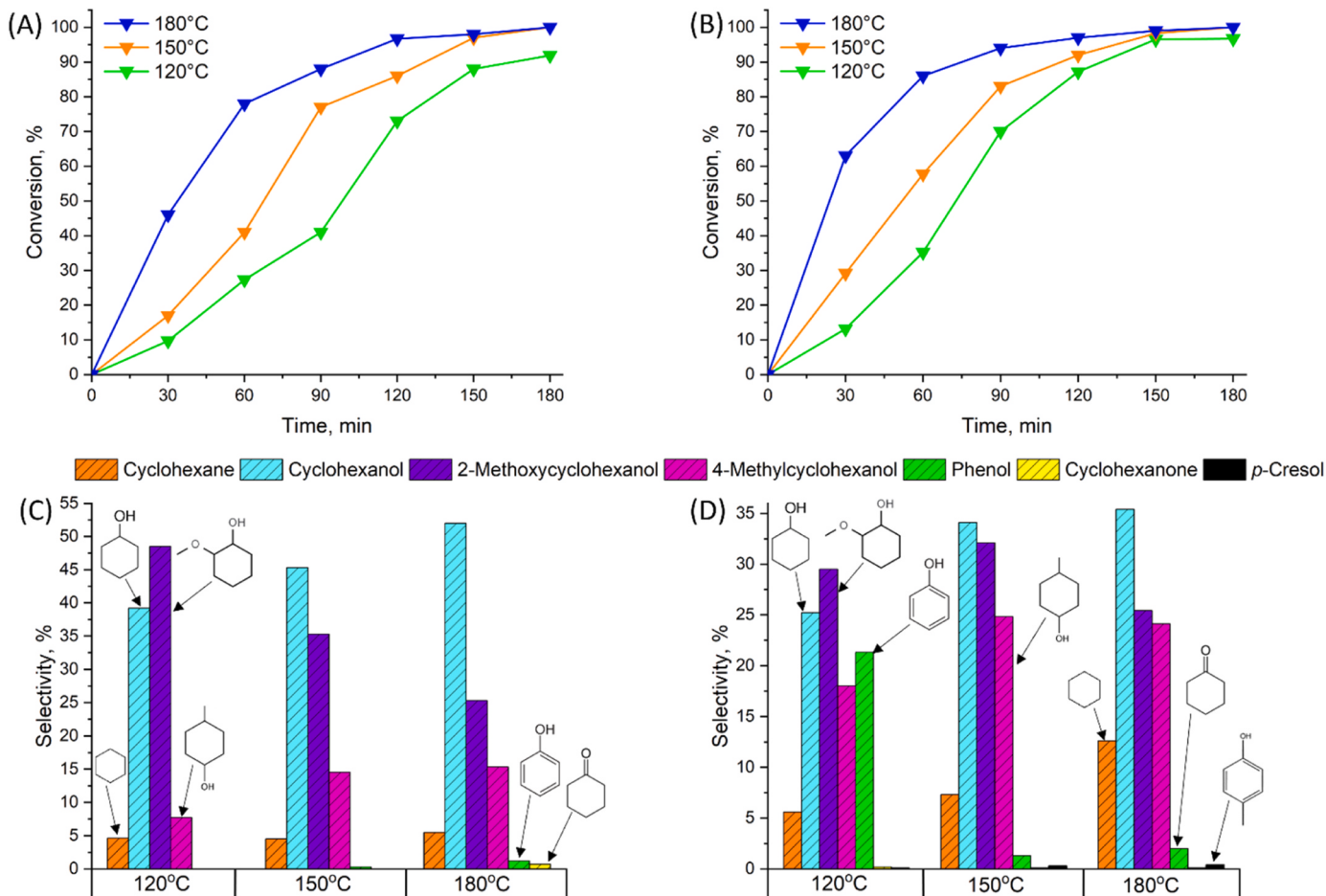


Fig. 7. Conversion (A, B) and selectivity (C, D) of guaiacol HDO as a function of time (A, B) and temperature (C, D) over Ru/HNT (A, C) and Ru/HNT-t (3) (B, D) catalysts. Reaction conditions: time = 3 h, H₂ pressure = 3 MPa, guaiacol/Ru ratio = 200, 10% wt. guaiacol water solution.

EDX elemental maps (Figs. 5,6 F-H) reveal Al, Si, and Ru components. It can be clearly confirmed that in the case of dealuminated sample, the amount of ruthenium nanoparticles is greater compared to the Ru/HNT sample. This observation also proves the acid etching considerably enhance the efficiency of tubes' loading due to increasing the inner space available for intercalation of ruthenium nanoparticles.

The H₂-TPR profiles for the Ru/HNT and Ru/HNT-t (3) samples and the quantification data are presented in Fig. S2 and Table 4, respectively. The ruthenium content was determined based on hydrogen consumption during the reduction of RuO_x particles. For all the samples, the maximum hydrogen uptake is in the temperature range of 130–160 °C (Fig. S2), indicating that the ruthenium nanoparticles are deposited on the outer and inner surfaces. This observation is in full agreement with TEM images (Figs. 5,6). The peaks on the H₂-TPR curve are symmetric and their broadening is attributed to stepwise reduction of RuO_x bounded with silanol and alumina groups to form Ru⁰. For Ru/HNT catalyst, the reduction peak is observed at 132 °C, which confirms the localization of ruthenium nanoparticles mainly on the outer surface of the halloysite [37]. This is also revealed on TEM micrographs (Fig. 5). In the case of Ru/HNT-t (3) sample the profile of the reduction curve is similar, but the peak maximum is shifted towards higher temperature (157 °C). It may be caused by the stronger interaction of RuO_x nanoparticles with alumina which form the internal surface of halloysite [35]. Thus, the enlargement of lumen diameter by selective acid dealumination provides an increase in the loading of Ru nanoparticles into inner cavity of halloysite. This fact is in agreement with the ruthenium content calculated from the H₂-TPR data (Table 4). Also, it should be noted that the ruthenium content calculated from the TPR data is in a full agreement with that measured by the X-ray fluorescence spectroscopy (Table 3) and the distinction between the values is less than 5%.

3.3. Catalytic activity tests

Catalytic behavior of the supported on pristine HNT and acid-etched HNT (HNT-t (3)) catalysts decorated with ruthenium was evaluated in HDO of model feed (10 wt% guaiacol in water) under H₂ pressure of 3 MPa in the temperature range of 120–180 °C for 3 h with a molar guaiacol/Ru ratio of 200. Fig. 7 summarizes the results of guaiacol HDO depending on reaction conditions, i.e. temperature and time. As demonstrated on Fig. 7A, guaiacol conversion over Ru/HNT catalyst was 92% at 120 °C and increased up to 100% with heating even to 150 °C. For low-acid pristine HNTs-supported Ru catalysts, cyclohexanol and 2-methoxycyclohexanol were detected as the major products (Fig. 7C), and selectivity to cyclohexanol reaches 52%. So that, one may conclude, that guaiacol transforms through hydrogenation of aromatic ring predominantly, and no C-O bond cleavage of polar group occurs [38]. Meanwhile, under the typical conditions (3 MPa H₂, 180 °C, 3 h), the Ru/HNT catalyst provides the efficient HDO of guaiacol, and TOF values reaches 95 h⁻¹. In view of product distribution, Ar-OCH₃ bond was preferentially cleaved from guaiacol prior to Ar-OH bond scission. These results are in accordance with computational chemistry calculations of the bond dissociation energies being for Ar-OCH₃ and Ar-OH in guaiacol equal to 375 kJ/mol and 456 kJ/mol, respectively [39]. In addition, the high selectivity to cyclohexanone and 2-methoxycyclohexanol during HDO of guaiacol suggested that hydrogenation and demethylation occurs simultaneously, and at relatively low temperatures these reaction pathways are prior to dehydroxylation. The reaction temperature significantly affects the distribution of guaiacol HDO products (Fig. 7). At 120 °C the 2-methoxycyclohexanol was detected as the major product of guaiacol HDO over Ru/HNT catalyst with 48.5% selectivity, and that decreases with temperature. Opposed to 2-methoxycyclohexanol, on rising the temperature, the content of cyclohexanol increases and reaches maximum value at 180 °C. Therefore, one may conclude, that cyclohexanol forms not only through phenol hydrogenation, but also during demethylation of 2-methoxycyclohexanol.

Despite the high conversion of guaiacol, the effectiveness of oxygen

Table 5
Results of blank experiments.

Sample	T, °C	Conversion, %	Selectivity, %		
			Anisole	Phenol	p-Cresol
HNT	120	4.2	24.7	75.3	-
	150	6.8	26.4	73.6	-
	180	9.3	29.2	70.8	-
HNT-t (3)	120	6.9	28.1	71.9	-
	150	13.1	26.1	72.7	1.2
	180	17.4	22.3	76.0	1.7

Reaction conditions: time = 3 h, H₂ pressure = 3 MPa, 60 mg of support, 10% wt. guaiacol water solution

removal, i.e. selectivity to non-oxygen-containing products was not too high. Thus, the selectivity for cyclohexane was only 6% at 180 °C (Fig. 7C). This result was expected for pristine HNTs-supported Ru catalysts due to the low acidity (0.131 mmol/g), which is not higher enough to provide hydrogenolysis of C-O bond. At 180 °C the yield of by-products (4-methylcyclohexanol) formed through the transalkylation mechanism increases. Supposedly, transalkylation may occur over aluminum atoms exhibiting acceptor properties (Lewis acid sites). Aluminum accepts a vacant p-electron pair from an oxygen atom, forming weak coordination bond followed by a heterolytic break of O-CH₃ bond. Afterwards, HNTs, which possess weak acid sites, provides alkylation of aromatic ring [3]. This result is not unusual for liquid-phase HDO catalyzed by bifunctional catalysts with high amount of Lewis acid sites [40,41].

As for Ru-catalyst based on acid-etched HNT (Ru/HNT-t (3)), it exhibits the higher activity in guaiacol HDO compared to Ru/HNT sample, revealing maximum TOF value of 211 h⁻¹ at 180 °C (Fig. 7B). This catalyst was more efficient towards hydrocarbons formation, and selectivity to cyclohexane reaches 12.6% at 100% guaiacol conversion (Fig. 7D) over the entire temperature range except 120 °C. Hydrogenation of aromatic ring during HDO of guaiacol over Ru/HNT-t (3) catalyst at 180 °C also occurred with high selectivity to cyclohexanol (35%), but still less than for Ru/HNT. A similar trend was observed to 2-methylcyclohexanol, too. Higher selectivity for cyclohexane in comparison to that for Ru/HNT counterpart is determined by the greater amount of acid sites in the HNT-t (3) support (0.343 mmol/g). However, dehydration of guaiacol was rather slow due to a high bond dissociation energy required for removal of hydroxyl group from guaiacol molecule as above mentioned.

For Ru/HNT-t (3) catalyst, an increased yield of 4-methylcyclohexanol with selectivity of 25% was observed, which is similar to that over Ru/HNT at 180 °C (Fig. 7D). It may be caused by the high amount of strong acid sites in HNT-t (3) dealuminated support (Table 1), which facilitate transalkylation reaction. Based on the product distribution it was also supposed that transalkylation occurred alongside hydrogenation and hydrogenolysis. This assumption was confirmed by a significant yield of phenol and a trace amount of p-cresol over Ru/HNT-t (3) at 120 °C (Fig. 7D). These results suggest that temperature is one of the key factors determining catalyst activity in transalkylation. Besides, a small amount of cyclohexanone (selectivity – 0.7%) was revealed in the reaction products (Fig. 7D), indicating that generated cyclohexanone was successively converted into cyclohexanol. Despite the high selectivity to reaction by-products, transalkylation occurring after demethylation is beneficial for carbon efficiency [42] and is typical for catalysts with acid function. An increased yield of transalkylation products may be not only due to high amount of acid sites, but also caused by peculiar reaction conditions, in particular, guaiacol transformation in aqueous media. It can be accompanied by protons formation increasing the acidity of reaction media [43].

To evaluate the impact of support and active component on reaction pathway of guaiacol transformation, the blank experiments (using supports without active phase loaded) were performed (Table 5). According

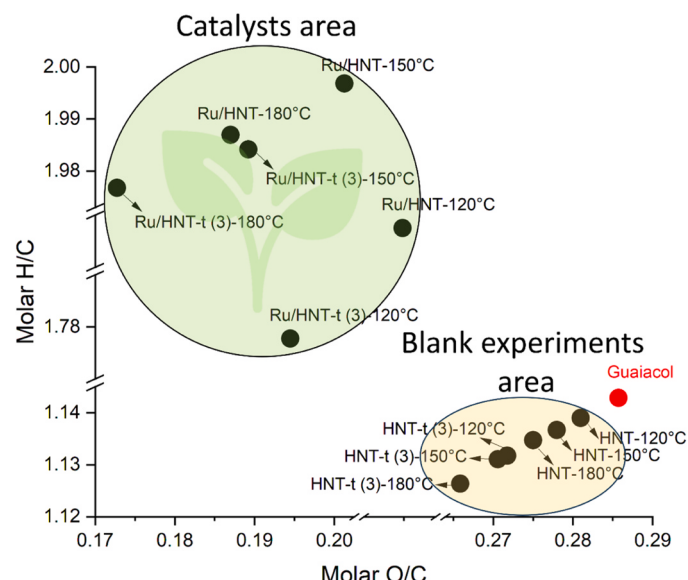


Fig. 8. Van Krevelen plot for guaiacol HDO products over Ru/HNT and Ru/HNT-t (3) catalysts and HNT, HNT-t (3) supports at different temperatures.

to the product distribution, phenol and anisole were the major products and small amounts of *p*-cresol were detected when using HNT-t (3) dealuminated support. When the temperature rising up to 180 °C the selectivity to anisole increases as compared to the experiments at 120 °C. The obtained data confirm the influence of acidity of the acid etched support (HNT-t (3)) on the distribution of the reaction products. Thus, for catalyst based on low-acid support (pristine HNTs) dehydration of phenyl ring is inhibited due to a higher bond dissociation energy required for the aromatic hydroxyl detachment compared to that of methoxyl group [39]. Formation of toluene and *p*-cresol over Ru/HNT-t

(3) suggests that transalkylation reactions take place during the guaiacol HDO.

The Van Krevelen plot illustrates the efficiency of guaiacol HDO over pristine HNTs-based supports and the corresponding Ru-containing catalysts (Fig. 8). For so-called “blank” test, when the pristine HNTs supports, inc. HNTs being treated with sulfuric acid, were used as a catalyst for guaiacol transformation, the O/C and H/C molar ratios are practically unchanged independently from temperature. As for Ru catalyst supported both for unmodified and acid-treated HNTs, the O/C molar ratio decreases, whereas H/C increases with temperature. Thus, HDO of guaiacol at 180 °C under H₂ pressure of 3 MPa for 3 h over Ru catalysts based on HNT-derived supports provides a significant increase of the H/C (from 1.14 to 1.99) and a decline in the O/C molar ratio (from 0.29 to 0.17) compared to guaiacol. Within the type of the support, the highest H/C ratio achieves at 150 °C, and Ru/HNT catalyst reveal the enhanced hydrogenation activity as compared to HNT-t (3)-supported counterparts at this temperature. On rising the temperature to 180 °C, the H/C ratio decreases slightly for catalysts of both types, whereas a deoxygenation increases significantly. In view of H/C and O/C ratios, one may conclude, that increasing the temperature from 120 °C to 150 °C affects on hydrogen saturation predominantly, whereas above 150 °C the temperature favors an oxygen removal.

Notably, that despite the difference in product distribution for Ru/HNT and Ru/HNT-t (3) catalysts, it demonstrates the similar results for H/C and O/C ratios at 180 °C and 150 °C, respectively. From standpoint of the Van Krevelen plot is the indicator of HDO efficiency, one should bear in mind that even cyclohexanol, 2-methoxycyclohexanol and 4-methylcyclohexanol are high-value products which can be blended with petroleum to benefit for O/C and H/C ratio.

Based on the above discussed product distribution depending on temperature and time (Fig. 7C-D), the possible pathways for HDO of guaiacol over halloysite-based catalyst was proposed. As shown in Fig. 9, at the initial step guaiacol transforms via two parallel pathways: (I) hydrogenation reaction route, where guaiacol converted to 2-methoxycyclohexanol; (II) direct deoxygenation, involving the cleavage of CH₃O-

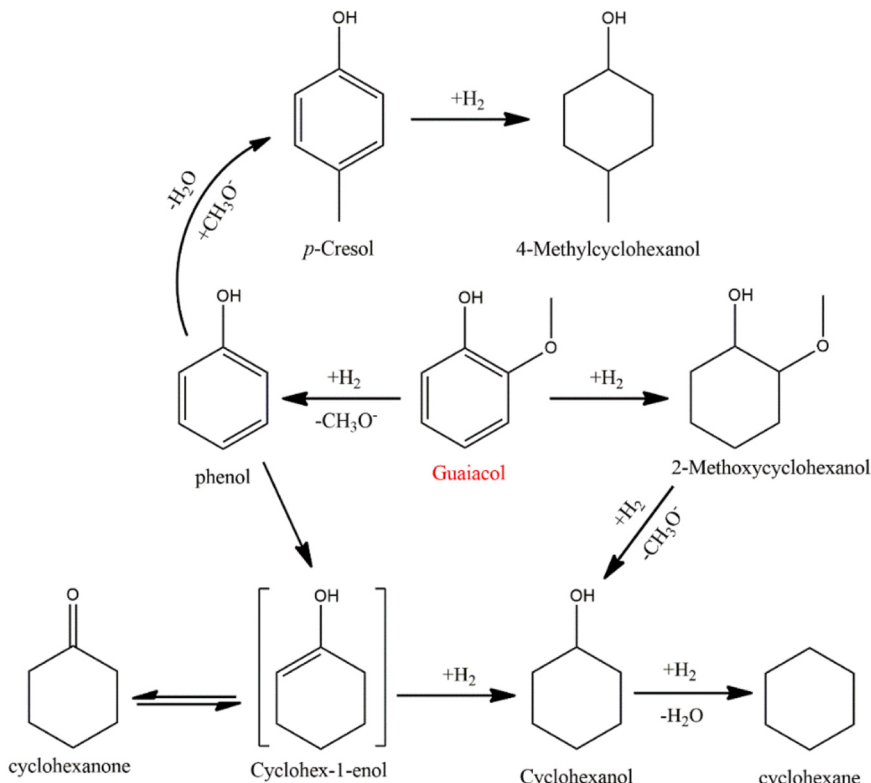


Fig. 9. Possible pathways for the HDO reaction of guaiacol over Ru/HNT and Ru/HNT-t (3) catalysts.

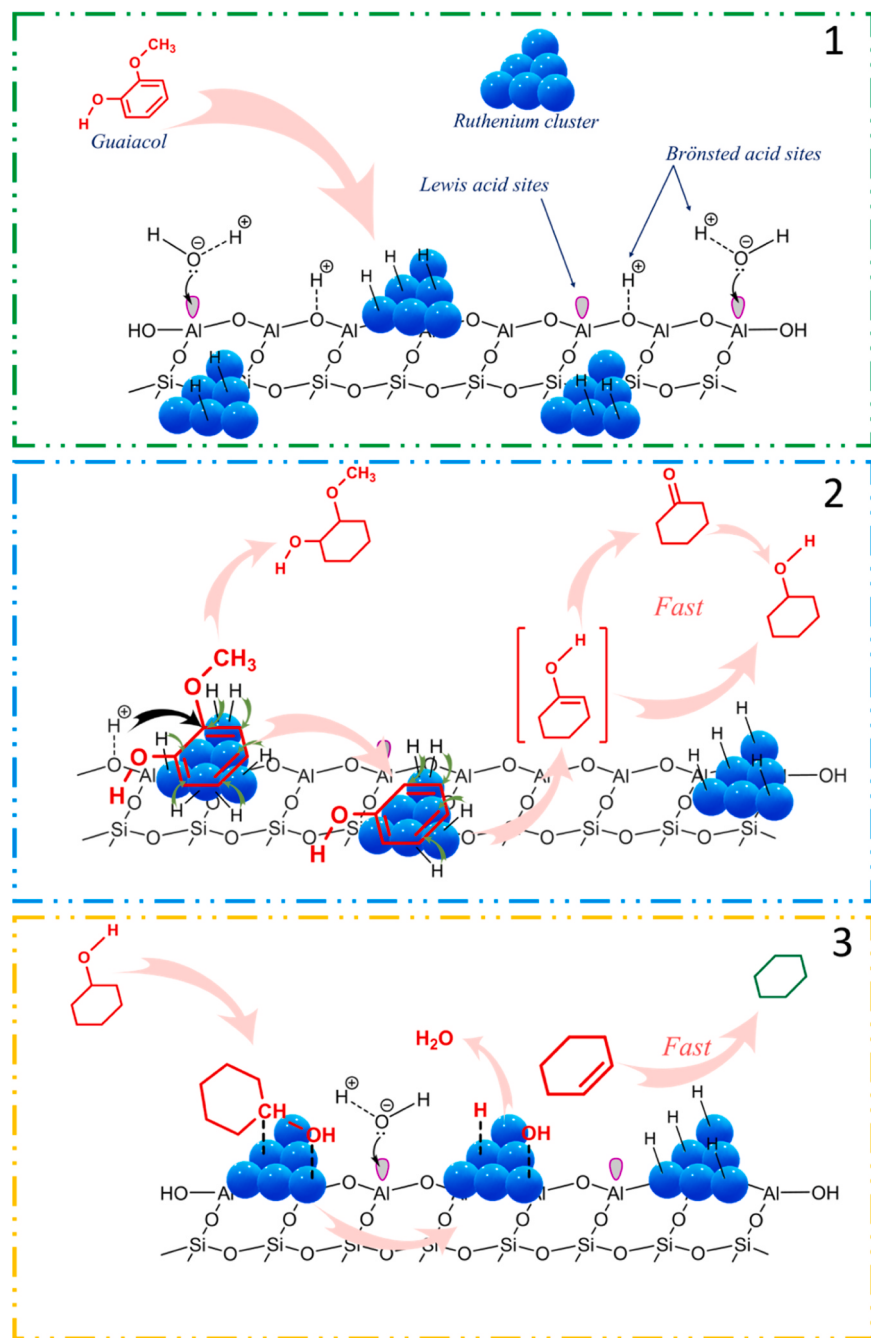


Fig. 10. Proposed reaction mechanism for HDO of guaiacol over a halloysite-supported Ru-catalysts (represented schematically).

, i.e. demethoxylation to phenol [44]. The increased content of 2-methoxycyclohexanol and cyclohexanol indicates, that guaiacol transforms through the hydrogenation of aromatic ring predominantly, and no functional groups were affected. However, for the catalyst supported on dealuminated halloysite, the impact of transalkylation and hydrogenolysis products increased significantly. Probably, a strong-medium acid sites in Ru/HNT-t (3) catalyst were useful for dehydration reaction. But despite the high reaction temperature and the presence of more acidic support, hydrogenolysis was not the main pathway of guaiacol HDO.

Based on the results of catalysts-assisted and blank tests, a mechanism for the HDO of guaiacol over bifunctional HNTs-supported Ru catalysts was proposed (Fig. 10). At the first stage, the guaiacol molecule diffuses to the catalyst's surface, where the flat sorption of aromatic ring over metal sites occurs. In this case, oxygen-containing substituents may

also interact with surface hydroxyls and aluminum atoms (Brønsted and Lewis acid sites) through oxygen atom, which leads to the formation of phenolates as the main precursors to coke and poisons for metal active component [45,46]. Owing to the 2-methoxycyclohexanol was detected in the reaction products with high selectivity, the flat sorption of aromatic ring is more likely. So that, in the second step, the adsorbed guaiacol undergoes hydrogenation of the aromatic ring to form a complete reduction product (2-methoxycyclohexanol) without deoxygenation.

At the same time, guaiacol simultaneously undergoes an attack by the H^+ electrophiles in the most vulnerable position for energy reasons – $\text{C}-\text{OCH}_3$ (bond dissociation energy = 375 kJ/mol). As a result, an intermediate carbocation is formed, which stabilized when eliminating $\text{O}-\text{CH}_3$ group [47,48]. Following this, phenol formed after demethoxylation of guaiacol and transforms to cyclohexanol on metal sites. Since

Table 6

Catalytic behavior of ruthenium catalysts in HDO of guaiacol under biphasic conditions depending on the support.

Catalyst	Ru, wt%	T, °C	P (H ₂), bar	t, h	GUA/Ru (mol/mol)	Conv., %	Sel., %	Ref.
Ru/SiO ₂	3	180	20	4	452	100	cyclohexanol – 74.4 2-methoxycyclohexanol – 24.4 cyclohexanone – 0.9 cyclohexane – 0.2 others – 0.1	[50]
Ru/Al ₂ O ₃ -SiO ₂	3	180	20	4	452	100	cyclohexanol – 86.3 2-methoxycyclohexanol – 13.2 cyclohexane – 0.5	[50]
Ru/H-ZSM-5	0.5	140	40	8	203	99	2-methoxycyclohexanol – 51.4 cyclohexane – 48.6	[51]
Ru/HY	5	250	40	2	16	91	cyclohexane – 27.5 cyclohexane – 18.5 cyclohexanol – 18.1 gases – 10.0 ring-open products – 8.2 cyclopentylmethanol – 7.9 dimers – 6.3 others – 3.5	[52]
Ru/Al-HMS	1	200	50	3	163	85	cyclohexane – 62.0 methylcyclohexane – 15.0 cyclohexanol – 11.0 2-methoxycyclohexanol – 8.0 phenol – 3.0 p-cresol – 1.0	[53]
Ru/HNT-t (3)	2	180	30	3	200	100	cyclohexanol – 35.4 2-methoxycyclohexanol – 25.4 4-methylcyclohexanol – 24.1 cyclohexane – 12.6 phenol – 2.0 p-cresol – 0.4 cyclohexanone – 0.1	This article

cyclohexane was detected in the reaction products, we assumed that the cyclohexanol formed at the metal sites through the adsorption of the OH group [49]. The actual deoxygenation step probably occurs through a dehydration of cyclohexanol with the formation of cyclohexene, which subsequently can be hydrogenated into cyclohexane as the final product.

Based on the literature review on evaluation of catalytic behavior of Ru-containing samples in HDO of guaiacol in water, i.e. under biphasic conditions, depending on support, one may conclude the Ru/HNT-t (3) catalyst is no less activity as compared to reported analogous (Table 6).

The Ru catalyst supported on dealuminated halloysite provides the complete conversion of guaiacol, whereas the application of zeolite- and mesoporous aluminosilicates-based counterparts (Ru/H-ZSM-5, Ru/HY, Ru/Al-HMS) are failed to achieve 100% conversion. Ru/HNT-t (3) catalyst was more efficient in the formation of hydrocarbons, particularly cyclohexane, than silica- and alumina-based analogous. Moreover, the natural clay nanotubes are more preferable as support for Ru catalysts from the standpoint of their costs as compared to synthetic aluminosilicates and zeolites.

4. Conclusions

In this study the HDO of guaiacol over ruthenium-catalysts based on natural halloysite nanotubes was thoroughly investigated. In general, acid treatment of halloysite had a positive impact on physicochemical properties such as a lumen diameter (24.3 nm), specific surface area (154 m²/g), acidity (0.343 mmol/g) and activity (211 h⁻¹) of Ru-catalysts in liquid-phase HDO. For Ru/HNT catalyst guaiacol transforms through the hydrogenation of aromatic ring with preservation of the polar group resulted in cyclohexanol and 2-methoxycyclohexanol formation as the major products. In addition to the 100% guaiacol conversion over the whole temperature and reaction time range, the Ru/HNT-t (3) catalyst demonstrated an increased selectivity to entirely deoxygenated products (cyclohexane). This result was attributed to the increased acidity of the etched support (HNT-t (3)) compared to the pristine halloysite. For both catalysts an increased yield of guaiacol HDO by-products (4-methylcyclohexanol) was observed. This can be

explained by the transalkylation reaction. The product distribution results are in full agreement with the blank experiments data. Significant amount of 4-methylcyclohexanol is not a negative result, since it, like cyclohexane, favorably affects the H/C and O/C molar ratio.

This pioneered research on HDO catalysts supported on natural clay nanotubes implies not only understanding of guaiacol transformation but boosting R&D efforts for transposition these systems for bio-oils processing. Halloysite nanotubes are available in thousand tons worldwide and can be easily scaled up for industrial application.

Funding

This work was financially supported by the Russian Science Foundation (Project No. 19-79-10016, <https://rsrf.ru/project/22-79-41047/>).

CRedit authorship contribution statement

Gleb Zasypalov: Investigation, Software, Methodology, Writing – original draft, Writing – review & editing. **Anna Vutolkina:** Validation, Data curation, Conceptualization, Writing – review & editing. **Vladimir Klimovsky:** Software, Writing – review & editing. **Egor Abramov:** Visualization, Software. **Vladimir Vinokurov:** Formal analysis, Resources. **Aleksandr Glotov:** Conceptualization, Writing – review & editing, Supervision, Project administration, Funding acquisition.

Declaration of Competing Interest

The authors declare that they have no known competing financial interests or personal relationships that could have appeared to influence the work reported in this paper.

Data Availability

Data will be made available on request.

Acknowledgments

The authors thank Dr. K. Cherednichenko, Ms. M. Reshetina and Mr. N. Vinogradov for physicochemical data and for technical help. The authors thank Lomonosov Moscow State University Program of Development for guaiacol products identification by mass-spectrometry.

Appendix A. Supporting information

Supplementary data associated with this article can be found in the online version at [doi:10.1016/j.apcatb.2023.123425](https://doi.org/10.1016/j.apcatb.2023.123425).

References

- [1] G. Kabir, B.H. Hameed, Recent progress on catalytic pyrolysis of lignocellulosic biomass to high-grade bio-oil and bio-chemicals, *Renew. Sustain. Energy Rev.* 70 (2017) 945–967, <https://doi.org/10.1016/J.RSER.2016.12.001>.
- [2] P.M. Mortensen, J.D. Grunwaldt, P.A. Jensen, K.G. Knudsen, A.D. Jensen, A review of catalytic upgrading of bio-oil to engine fuels, *Appl. Catal. A Gen.* 407 (2011) 1–19, <https://doi.org/10.1016/J.APCATA.2011.08.046>.
- [3] P. Mäki-Arvela, D. Murzin, Hydrodeoxygenation of Lignin-Derived Phenols: From Fundamental Studies towards Industrial Applications, *Catalysts* 7 (2017) 265, <https://doi.org/10.3390/catal7090265>.
- [4] Q.K. Tran, S. Han, H.V. Ly, S.S. Kim, J. Kim, Hydrodeoxygenation of a bio-oil model compound derived from woody biomass using spray-pyrolysis-derived spherical γ -Al2O3-SiO2 catalysts, *J. Ind. Eng. Chem.* 92 (2020) 243–251, <https://doi.org/10.1016/J.JIEC.2020.09.012>.
- [5] C. Zhao, S. Kasakov, J. He, J.A. Lercher, Comparison of kinetics, activity and stability of Ni/HZSM-5 and Ni/Al2O3-HZSM-5 for phenol hydrodeoxygenation, *J. Catal.* 296 (2012) 12–23, <https://doi.org/10.1016/J.JCAT.2012.08.017>.
- [6] K.L. Deutsch, B.H. Shanks, Hydrodeoxygenation of lignin model compounds over a copper chromite catalyst, *Appl. Catal. A Gen.* 447–448 (2012) 144–150, <https://doi.org/10.1016/J.APCATA.2012.09.047>.
- [7] J. Lu, S. Behtash, O. Mamun, A. Heyden, Theoretical Investigation of the Reaction Mechanism of the Guaiacol Hydrogenation over a Pt(111) Catalyst, *ACS Catal.* 5 (2015) 2423–2435, <https://doi.org/10.1021/cs5016244>.
- [8] Y. Xin, Z. Zheng, Z. Luo, C. Jiang, S. Gao, Z. Wang, C. Zhao, The influence of pore structures and Lewis acid sites on selective hydrogenolysis of guaiacol to benzene over Ru/TS-1, *Green. Energy Environ.* 7 (2022) 1014–1023, <https://doi.org/10.1016/J.GEE.2020.12.024>.
- [9] H. Lee, H. Kim, M.J. Yu, C.H. Ko, J.K. Jeon, J. Jae, S.H. Park, S.C. Jung, Y.K. Park, Catalytic Hydrodeoxygenation of Bio-oil Model Compounds over Pt/HY Catalyst, *Sci. Rep.* 6 (2016), <https://doi.org/10.1038/srep28765>.
- [10] Z. Zhang, Y. Zhu, H. Asakura, B. Zhang, J. Zhang, M. Zhou, Y. Han, T. Tanaka, A. Wang, T. Zhang, N. Yan, Thermally stable single atom Pt/m-Al2O3 for selective hydrogenation and CO oxidation, *Nat. Commun.* 8 (2017), <https://doi.org/10.1038/ncomms16100>.
- [11] E.R. Naranov, A.A. Sadovnikov, O.V. Arapova, A.L. Bugaev, O.A. Usoltsev, D. N. Gorbunov, V. Russo, D.Yu Murzin, A.L. Maximov, Mechanistic insights on Ru nanoparticle in situ formation during hydrodeoxygenation of lignin-derived substances to hydrocarbons, *Catal. Sci. Technol.* 13 (2023) 1571–1583, <https://doi.org/10.1039/D2CY01127A>.
- [12] A.P. Glotov, A.V. Vutolkina, N.A. Vinogradov, A.A. Pimerzin, V.A. Vinokurov, A.I. Pimerzin, Enhanced HDS and HYD activity of sulfide Co-PMo catalyst supported on alumina and structured mesoporous silica composite, *Catal. Today* 377 (2021) 82–91, <https://doi.org/10.1016/j.cattod.2020.10.010>.
- [13] Y.H. Kang, X.Y. Wei, G.H. Liu, Y. Gao, Y.J. Li, X.R. Ma, Z.F. Zhang, Z.M. Zong, Catalytic hydroconversion of soluble portion in the extraction from Hecaogou subbituminous coal to clean liquid fuel over a Y/ZSM-5 composite zeolite-supported nickel catalyst, *Fuel* 269 (2020), 117326, <https://doi.org/10.1016/J.FUEL.2020.117326>.
- [14] J. Zhang, A. Dasgupta, Z. Chen, D. Xu, P.E. Savage, Y. Guo, Supercritical water gasification of phenol over Ni-Ru bimetallic catalysts, *Water Res* 152 (2019) 12–20, <https://doi.org/10.1016/J.WATRES.2018.12.030>.
- [15] E. Karakhanov, A. Maximov, A. Zolotukhina, A. Mamadli, A. Vutolkina, A. Ivanov, Dendrimer-Stabilized Ru Nanoparticles Immobilized in Organo-Silica Materials for Hydrogenation of Phenols, *Catalysts* 7 (2017) 86, <https://doi.org/10.3390/catal7030086>.
- [16] E. Naranov, A. Sadovnikov, O. Arapova, T. Kuchinskaya, O. Usoltsev, A. Bugaev, K. Janssens, D. De Vos, A. Maximov, The in-situ formation of supported hydrous ruthenium oxide in aqueous phase during HDO of lignin-derived fractions, *Appl. Catal. B* 334 (2023), 122861, <https://doi.org/10.1016/J.APCATB.2023.122861>.
- [17] A. Glotov, A. Vutolkina, A. Pimerzin, V. Nedolivko, G. Zasypalov, V. Stytsevko, E. Karakhanov, V. Vinokurov, Ruthenium catalysts templated on mesoporous MCM-41 type silica and natural clay nanotubes for hydrogenation of benzene to cyclohexane, *Catalysis* 10 (2020) 537, <https://doi.org/10.3390/catal10050537>.
- [18] E.R. Naranov, A.A. Sadovnikov, A.L. Bugaev, D.A. Shavaleev, A.L. Maximov, A stepwise fabrication of MF nanosheets in accelerated mode, *Catal. Today* 378 (2021) 149–157, <https://doi.org/10.1016/j.cattod.2021.06.011>.
- [19] X. Jiang, J. Zhou, J. Zhao, D. Shen, Catalytic conversion of guaiacol as a model compound for aromatic hydrocarbon production, *Biomass Bioenergy* 111 (2018) 343–351, <https://doi.org/10.1016/J.BIOMBIOE.2017.06.026>.
- [20] Y. Lvov, A. Panchal, Y. Fu, R. Fakhrullin, M. Kryuchkova, S. Batasheva, A. Stavitskaya, A. Glotov, V. Vinokurov, Interfacial self-assembly in halloysite nanotube composites, *Langmuir* 35 (2019) 8646–8657, <https://doi.org/10.1021/acs.langmuir.8b04313>.
- [21] L. Fu, H. Yang, A. Tang, Y. Hu, Engineering a tubular mesoporous silica nanocontainer with well-preserved clay shell from natural halloysite, *Nano Res.* 10 (2017) 2782–2799, <https://doi.org/10.1007/s12274-017-1482-x>.
- [22] A. Glotov, A. Vutolkina, A. Pimerzin, V. Vinokurov, Y. Lvov, Clay nanotube-metal core/shell catalysts for hydroprocesses, *Chem. Soc. Rev.* 50 (2021) 9240–9277, <https://doi.org/10.1039/dlcs00502b>.
- [23] V. Vinokurov, A. Glotov, Y. Chudakov, A. Stavitskaya, E. Ivanov, P. Gushchin, A. Zolotukhina, A. Maximov, E. Karakhanov, Y. Lvov, Core/Shell ruthenium-halloysite nanocatalysts for hydrogenation of phenol, *Ind. Eng. Chem. Res* 56 (2017) 14043–14052, <https://doi.org/10.1021/acs.iecr.7b03282>.
- [24] N.R. Demikhova, S.S. Boev, M.V. Reshetina, K.A. Cherednichenko, V.A. Vinokurov, A.P. Glotov, Micro-mesoporous catalyst based on dealuminated halloysite nanotubes for isomerization of C-8 aromatic fraction, *Pet. Chem.* 61 (2021) 1085–1095, <https://doi.org/10.1134/S0965544121100030>.
- [25] V.V. Nedolivko, G.O. Zasypalov, S.S. Boev, K.A. Cherednichenko, V.A. Vinokurov, A.P. Glotov, Ruthenium-containing catalysts based on halloysite aluminosilicate nanotubes of different origin in benzene hydrogenation, *Pet. Chem.* 61 (2021) 1104–1110, <https://doi.org/10.1134/S0965544121100017>.
- [26] E. Abdullayev, A. Joshi, W. Wei, Y. Zhao, Y. Lvov, Enlargement of halloysite clay nanotube lumen by selective etching of aluminum oxide, *ACS Nano* 6 (2012) 7216–7226, <https://doi.org/10.1021/nn302328x>.
- [27] S. Lim, S. Park, D. Sohn, Modification of halloysite nanotubes for enhancement of gas-adsorption capacity, *Clays Clay Min.* 68 (2020) 189–196, <https://doi.org/10.1007/s42860-019-00059-4>.
- [28] J.M. Falcón, T. Sawczew, I.V. Aoki, Dodecylamine-loaded halloysite nanocontainers for active anticorrosion coatings, *Front Mater.* 2 (2015), <https://doi.org/10.3389/fmats.2015.00069>.
- [29] A.V. Vutolkina, I.G. Baigildin, A.P. Glotov, A.A. Pimerzin, A.V. Akopyan, A. L. Maximov, E.A. Karakhanov, Hydrodeoxygenation of guaiacol via in situ H₂ generated through a water gas shift reaction over dispersed NiMoS catalysts from oil-soluble precursors: tuning the selectivity towards cyclohexene, *Appl. Catal. B* 312 (2022), 121403, <https://doi.org/10.1016/J.APCATB.2022.121403>.
- [30] K. Belkassa, M. Khelifa, I. Batonneau-Gener, K. Marouf-Khelifa, A. Khelifa, Understanding of the mechanism of crystal violet adsorption on modified halloysite: Hydrophobicity, performance, and interaction, *J. Hazard. Mater.* 415 (2021), 125656, <https://doi.org/10.1016/J.JHAZMAT.2021.125656>.
- [31] H. Shao, J. Chen, J. Zhong, Y. Leng, J. Wang, Development of MeSAPO-5 molecular sieves from attapulgite for dehydration of carbohydrates, *Ind. Eng. Chem. Res* 54 (2015) 1470–1477, <https://doi.org/10.1021/ie504243t>.
- [32] S. Chen, W. Wang, X. Li, P. Yan, W. Han, T. Sheng, T. Deng, W. Zhu, H. Wang, Regulating the nanoscale intimacy of metal and acidic sites in Ru/γ-Al2O3 for the selective conversions of lignin-derived phenols to jet fuels, *J. Energy Chem.* 66 (2022) 576–586, <https://doi.org/10.1016/j.jechem.2021.08.058>.
- [33] G. Leofanti, M. Padovan, G. Tozzola, B. Venturelli, Surface area and pore texture of catalysts, *Catal. Today* 41 (1998) 207–219, [https://doi.org/10.1016/S0920-5861\(98\)00509-4](https://doi.org/10.1016/S0920-5861(98)00509-4).
- [34] F. Bessaha, K. Marouf-Khelifa, I. Batonneau-Gener, A. Khelifa, Characterization and application of heat-treated and acid-leached halloysites in the removal of malachite green: adsorption, desorption, and regeneration studies, *Desalin. Water Treat.* 57 (2016) 14609–14621, <https://doi.org/10.1080/19443994.2015.1063090>.
- [35] A. Glotov, A. Novikov, A. Stavitskaya, V. Nedolivko, D. Kopitsyn, A. Kuchierskaya, E. Ivanov, V. Stytsevko, V. Vinokurov, Y. Lvov, Nanoreactors based on hydrophobized tubular aluminosilicates decorated with ruthenium: Highly active and stable catalysts for aromatics hydrogenation, *Catal. Today* 378 (2021) 33–42, <https://doi.org/10.1016/j.cattod.2020.10.001>.
- [36] V.V. Nedolivko, G.O. Zasypalov, Ya.A. Chudakov, A.V. Pimerzin, A.P. Glotov, Effect of the ruthenium deposition method on the nanostructured catalyst activity in the deep hydrogenation of benzene, *Russ. Chem. Bull.* 69 (2020) 260–264, <https://doi.org/10.1007/s11172-020-2754-2>.
- [37] A.V. Vutolkina, G.O. Zasypalov, Ya Aljajan, V.A. Klimovsky, V.A. Vinokurov, M. I. Rubtsova, Al.A. Pimerzin, A.P. Glotov, Gram-scale ruthenium catalysts templated on halloysite nanotubes and MCM-41/halloysite composite for removal of aromatics from gasoline fraction, *New J. Chem.* 47 (2023) 12015–12026, <https://doi.org/10.1039/D3NJ01709E>.
- [38] Y. Xin, Z. Zheng, Z. Luo, C. Jiang, S. Gao, Z. Wang, C. Zhao, The influence of pore structures and Lewis acid sites on selective hydrogenolysis of guaiacol to benzene over Ru/TS-1, *Green. Energy Environ.* 7 (2022) 1014–1023, <https://doi.org/10.1016/J.GEE.2020.12.024>.
- [39] T. Prasomr, M. Shetty, K. Murugappan, Y. Román-Leshkov, Insights into the catalytic activity and surface modification of MoO₃ during the hydrodeoxygenation of lignin-derived model compounds into aromatic hydrocarbons under low hydrogen pressures, *Energy Environ. Sci.* 7 (2014) 2660–2669, <https://doi.org/10.1039/c4ee00890a>.
- [40] X. Zhu, L.L. Lobban, R.G. Mallinson, D.E. Resasco, Bifunctional transalkylation and hydrodeoxygenation of anisole over Pt/HBeta catalyst, *J. Catal.* 281 (2011) 21–29, <https://doi.org/10.1016/j.jcat.2011.03.030>.
- [41] X. Zhu, R.G. Mallinson, D.E. Resasco, Role of transalkylation reactions in the conversion of anisole over HZSM-5, *Appl. Catal. A Gen.* 379 (2010) 172–181, <https://doi.org/10.1016/j.apcata.2010.03.018>.

[42] J.E. Peters, J.R. Carpenter, D.C. Dayton, Anisole and guaiacol hydrodeoxygenation reaction pathways over selected catalysts, *Energy Fuels* 29 (2015) 909–916, <https://doi.org/10.1021/ef502551p>.

[43] H. Ohta, H. Kobayashi, K. Hara, A. Fukuoka, Hydrodeoxygenation of phenols as lignin models under acid-free conditions with carbon-supported platinum catalysts, *Chem. Commun.* 47 (2011) 12209–12211, <https://doi.org/10.1039/c1cc14859a>.

[44] J. Lu, S. Behtash, O. Mamun, A. Heyden, Theoretical investigation of the reaction mechanism of the guaiacol hydrogenation over a Pt(111) catalyst, *ACS Catal.* 5 (2015) 2423–2435, <https://doi.org/10.1021/cs5016244>.

[45] C. Zhao, S. Kasakov, J. He, J.A. Lercher, Comparison of kinetics, activity and stability of Ni/HZSM-5 and Ni/Al2O3-HZSM-5 for phenol hydrodeoxygenation, *J. Catal.* 296 (2012) 12–23, <https://doi.org/10.1016/j.jcat.2012.08.017>.

[46] Z. Wang, Y. Zeng, W. Lin, W. Song, In-situ hydrodeoxygenation of phenol by supported Ni catalyst – explanation for catalyst performance, *Int. J. Hydrog. Energy* 42 (2017) 21040–21047, <https://doi.org/10.1016/j.ijhydene.2017.07.053>.

[47] K. Lee, G.H. Gu, C.A. Mullen, A.A. Boateng, D.G. Vlachos, Guaiacol hydrodeoxygenation mechanism on Pt(111): Insights from density functional theory and linear free energy relations, *ChemSusChem* 8 (2015) 315–322, <https://doi.org/10.1002/cssc.201402940>.

[48] F. Morteo-Flores, A. Roldan, Mechanisms and Trends of Guaiacol Hydrodeoxygenation on Transition Metal Catalysts, *Front. Catal.* 2 (2022), <https://doi.org/10.3389/fctls.2022.861364>.

[49] P.M. Mortensen, J.D. Grunwaldt, P.A. Jensen, A.D. Jensen, Screening of catalysts for hydrodeoxygenation of phenol as a model compound for bio-oil, *ACS Catal.* 3 (2013) 1774–1785, <https://doi.org/10.1021/cs400266e>.

[50] M. Chen, Q. Zhong, M. Zhang, H. Huang, Y. Liu, Z. Wei, Aqueous phase partial hydrodeoxygenation of lignin-derived phenols over Al2O3-SiO2 microspheres supported RuMn multifunctional catalyst: Synergic effect among Ru, Mn and Al2O3-SiO2 support, *Catal. Commun.* 172 (2022), 106550, <https://doi.org/10.1016/j.catcom.2022.106550>.

[51] G. Yao, G. Wu, W. Dai, N. Guan, L. Li, Hydrodeoxygenation of lignin-derived phenolic compounds over bi-functional Ru/H-Beta under mild conditions, *Fuel* 150 (2015) 175–183, <https://doi.org/10.1016/j.fuel.2015.02.035>.

[52] H. Wang, H. Ruan, M. Feng, Y. Qin, H. Job, L. Luo, C. Wang, M.H. Engelhard, E. Kuhn, X. Chen, M.P. Tucker, B. Yang, One-Pot Process for Hydrodeoxygenation of Lignin to Alkanes Using Ru-Based Bimetallic and Bifunctional Catalysts Supported on Zeolite Y, *ChemSusChem* 10 (2017) 1846–1856, <https://doi.org/10.1002/cssc.201700160>.

[53] E.A. Roldugina, E.R. Naranov, A.L. Maximov, E.A. Karakhanov, Hydrodeoxygenation of guaiacol as a model compound of bio-oil in methanol over mesoporous noble metal catalysts, *Appl. Catal. A Gen.* 553 (2018) 24–35, <https://doi.org/10.1016/j.apcata.2018.01.008>.